2010 IEEE International Conference on Robotics and Automation
Anchorage Convention District
May 3-8, 2010, Anchorage, Alaska, USA

Non-ideal Swimming of Artificial Bacterial Flagella Near a Surface

Kathrin E. Peyer, Li Zhang, Bradley E. Kratochvil, and Bradley J. Nelson

Abstract— **The artificial bacterial flagellum (ABF), a helical swimming microrobot, has the potential to be used for biomedical applications such as cellular and intracellular manipulation. The velocity and the propulsive force of the ABF can be controlled by the input frequency of the rotating magnetic field. In this paper the swimming behavior of the ABF near a solid surface is reported. Three regions have been observed for the frequency-dependent swimming behavior of the ABF, i.e. the step-out, the linear and the drift-dominated region. At low frequencies it has been found that the desired screw-type motion is replaced by a wobbling swimming movement with a frequency-dependent precession angle. Moreover, the experimental results show that the wobbling motion of the ABF enhances the undesired sidewise drift due to wall effects. Additionally, the cause of the precession motion has been investigated by a hydrodynamic model. Our results imply that the linear range of the input magnetic frequency and the output ABF velocity is not only limited by the applicable torque at high frequencies but also by the wobbling of helical swimming at low frequencies.**

I. INTRODUCTION

Artificial bacterial flagella (ABFs) have the potential to be used for *in vivo* and *in vitro* biomedical applications such as cell manipulation and targeted drug delivery [1], [2]. An ABF uses a helical tail for propulsion and a soft-magnetic metal head for wireless actuation and steering (see Fig. 1). The velocity v and propulsive force F can be controlled by the input frequency f of the rotating magnetic field. Though helical swimmers have been investigated for more than a decade [3]–[5], the dimension of the robots has only recently been scaled down to nanometer range [1], [6]. By taking into account magnetic actuation and practicality in applications, helical swimming provides a number of advantages as a method of propulsion for swimming microrobots [7].

An ABF can act as a versatile microscopic wireless manipulator, making it desirable to have a linear relationship between the input frequency and the output velocity and force. Thus, in this paper we explorer the frequency−velocity relationship of helical swimming and the extent of its linear range. It is shown that the ABF wobbles at low input frequencies and the cause has been investigated using a hydrodynamic model based on the resistive force theory (RFT). The wobbling motion aggravates the non-ideal drifting behavior as the ABF swims near a solid surface. Experiments conducted in a microchannel demonstrate that the ABF is able to roll out of the channel due to the wobbling motion.

This work was supported in part by the Swiss National Science Foundation (SNSF).

The authors are with the Institute of Robotics and Intelligent Systems, ETH Zurich, 8092 Zurich, Switzerland {peyerk, lizhang, bkratochvil, bnelson}@ethz.ch

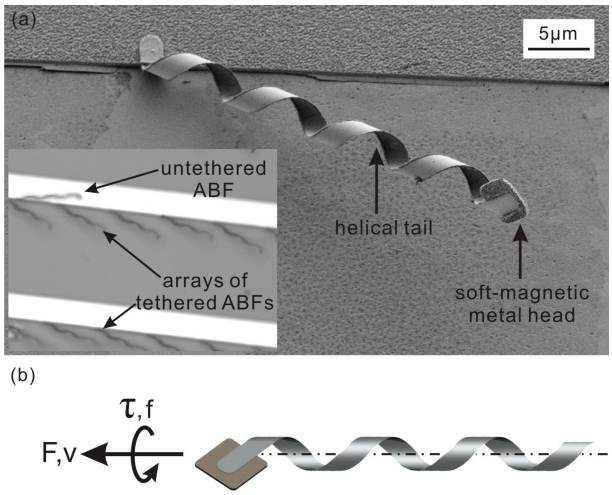

Fig. 1. (a) Field Emission Scanning Electron Microscope (FESEM) micrograph of an individual ABF consisting of a helical tail and a thin soft-magnetic metal head. Inset: Optical microscope image of a batch of tethered ABFs and an untethered ABF immersed in water. (b) Model of the ABF showing the actuation principle. By applying a torque the ABF is rotated along its helical axis and propelled forward by the helical tail.

The hydrodynamic model presented here verifies that the wobbling of ABF mainly results from two competing fluidic torques.

A. Fluid mechanics at low Reynolds numbers

An ABF swims in water at a low Reynolds number regime with $\mathrm{Re} = UL\rho/\eta < 10^{-3}$, where U and L are the velocity and characteristic length respectively, and ρ and η are the density and viscosity. The fluid mechanics at low Reynolds numbers can be described by the Stokes equations

$$\nabla p = \eta \nabla^2 \vec{V} + \vec{F} \quad (1)$$

$$\nabla \cdot \vec{V} = 0 \quad (2)$$

$\vec{V}$ is the velocity vector field, $\vec{F}$ is the body forces acting on the fluid and p is the scalar pressure field. Equation (2) represents the conservation of mass for an incompressible liquid.

In the Stokes equations the inertial terms are neglected and the flow is time-reversible. Microscopic swimmers, such as spermatozoa or bacteria, therefore, evolved swimming strategies that involve non-reciprocal movements in order to produce a displacement [8]. An ABF mimics the swimming style of bacterial swimmers, such as *E. coli*, which rotate helical flagella for propulsion [9].

B. Swimming with a helical tail

A screw-type swimming style can be achieved with a rotating helix where the rotary motion around the helical axis is translated into a linear motion. Unlike a screw, a helix in liquid does not advance at one pitch per rotation but instead slips through the liquid [8]. Purcell showed that the linear relationship between the forward velocity v, rotational speed ω, external force F and torque τ on a helix can be expressed in matrix form [8]

$$\begin{pmatrix} F \\ \tau \end{pmatrix} = \begin{pmatrix} A & B \\ B & C \end{pmatrix} \begin{pmatrix} v \\ \omega \end{pmatrix} \tag{3}$$

The matrix in (3) is also referred to as the "propulsion matrix". The head of the swimmer causes additional resistance to the flow, and its drag coefficients must be included. The head can be approximated by a sphere whose translational and rotational drag coefficients in Stokes flow are $D_v = 3\pi\eta d$ and $D_\omega = \pi\eta d^3$, respectively, in which η is the dynamic viscosity and d is the diameter of the sphere. Assuming that the flow around the sphere and the helical tail are independent of each other, D_v and D_ω may simply be added to A and C, respectively, which does not change the linearity of the equation.

II. METHODS

A. Fabrication

The ABF consists of a ribbon-like helical tail and a head that has the shape of thin square plate. The helical tail of the ABF is fabricated by the self-scrolling technique [10], [11]. The tail and the head consist of an InGaAs/GaAs/Cr trilayer and a Cr/Ni/Au trilayer respectively, patterned by photolithography. The mask design allows for different head sizes, ribbon widths, handedness and helicity angles of the ABF, while the film stiffness and internal stress influence the diameter of the helical tail. The details of the fabrication processes are reported in [1].

ABF prototypes used for the experiments in this paper have a head with dimensions 4.5 μm (length) $\times$ 4.5 μm (width) $\times$ 200 nm (thickness) and a ribbon width of 1.8 μm. The ribbon thickness is 42 nm and the diameter of the helix is 2.8 μm. Both left-handed and right-handed helical swimmers were fabricated. Additionally, microchannels were fabricated on a Si wafer: firstly, the Si wafer was spin-coated by a photoresist layer which was patterned with lines and then it was used as a mask for the reactive ion etching (RIE) process. The etching was isotropic and the resulting channel had a rounded cross-section with dimensions 120 μm (width) $\times$ 55 μm (depth).

B. Actuation of the ABF

The ABF is actuated by the rotation of a uniform low strength magnetic field with which a torque is applied to the soft-magnetic metal head (see Fig. 2 a). The torque on a magnetized body in a magnetic field is equal to

$$\vec{T}_m = \mu_0 \vartheta \vec{M} \times \vec{H} \tag{4}$$

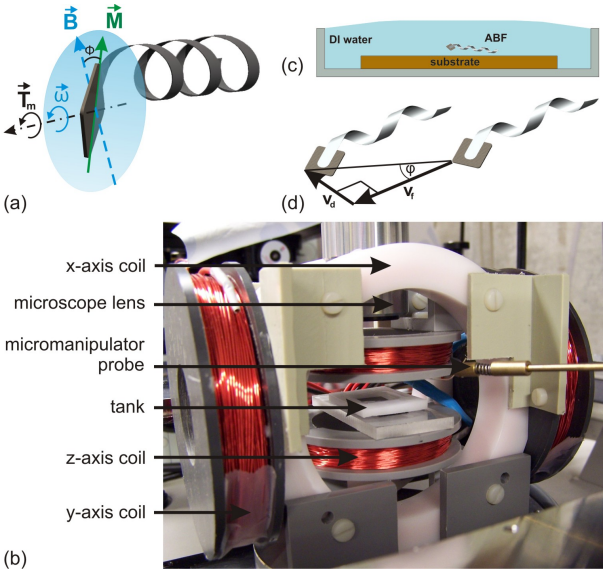

Fig. 2. (a) Application of the magnetic torque. The torque $\vec{\tau}$ is induced due to the misalignment between the magnetization $\vec{M}$ of the nickel plate, which is along its diagonal, and the external field vector $\vec{B}$. The magnetic field vector $\vec{B}$ is rotated in a plane perpendicular to the helical axis with a rotational speed $\vec{\omega}$. For a constant rotational speed the misalignment angle ϕ between $\vec{M}$ and $\vec{B}$ is constant. (b) Experimental Setup. The ABF swims inside the white tank which is placed in the middle of three orthogonal coil pairs. A micromanipulator is used to pick and place single ABFs. A camera mounted on the optical microscope is used for recording the motion of the ABF. (c) Schematic of the tank with ABF swimming above a Si substrate. (d) Forward and drift velocity. The drift angle φ is defined as the angle between the direction of the motion and the direction of the axis of the helical tail.

where ϑ and $\vec{M}$ are the volume and magnetization of the body respectively, and $\mu_0 = 4\pi \times 10^{-7}$ Tm/A is the permeability of free space. $\vec{H}$ is the applied field in units ampere per meter [12]. The magnetic field used during the experiments was $|\vec{B}| = \mu_0 |\vec{H}| = 2$ mT, approximately 1000 times less than typical MRI field strength. For actuating the ABF the field vector $\vec{B}$ is rotated in a plane perpendicular to the helical axis. The nickel layer of the head is magnetized along its diagonal and the magnitude of the torque grows with an increased angle ϕ between the nickel plate and the applied field. The ABF is steered by deviating the plane of rotation such that it is no longer perpendicular to the helical axis. A steering torque is induced and the ABF re-orients itself such that the plane of rotation is perpendicular to its helical axis again. The details of the actuation and steering are reported elsewhere [1]. When the available torque is large enough the ABF rotates in sync with the input frequency f and hence the velocity of the ABF can be tuned by changing the input frequency.

C. Experimental Setup

The rotating field is generated by three orthogonally-placed coil pairs which are depicted in Fig. 2 (b). The coils are placed under an optical microscope onto which a camera is mounted for recording. A tank with dimensions 20 mm (length) $\times$ 15 mm (width) $\times$ 2 mm (depth) is filled with DI water and placed in the middle of the coils. The substrate

with the ABF arrays is placed in the tank together with an Si substrate that provides either a flat surface or an array of microchannels (see Fig. 2 c). Using a micromanipulator probe an individual ABF is picked and placed above the Si substrate. The ABF remains attached to the probe while it is being transferred due to Van der Waal forces. After the ABF is released above the Si substrate by gently tapping the manipulator, the rotating field is switched on.

The velocity of the ABF was measured by driving the ABF for a time Δt at a constant frequency input and dividing the travelled distance by Δt. Imprecisions of the velocity measurements are attributed to the uncertainty of the distance and angle measurement on the recorded 480 $\times$ 640 pixel images. The velocity is projected into the directions parallel and perpendicular to the helical axis of the ABF. The desired direction of motion is in the direction of the helical axis, whereas the perpendicular component is labeled as drift velocity. The angle between the forward velocity and the actual direction of motion is the drift angle φ as shown in Fig. 2 (d).

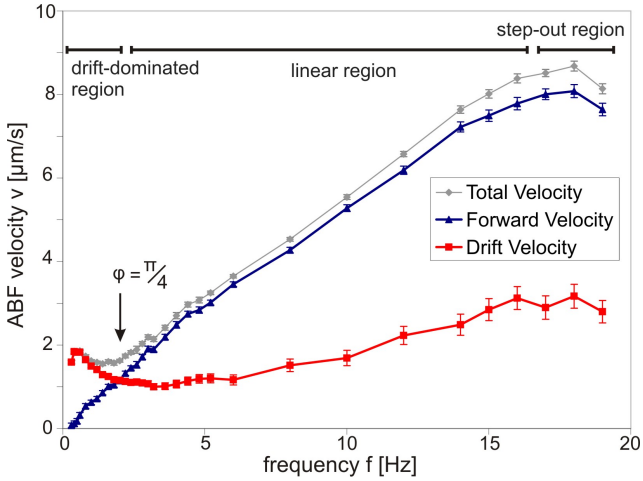

Fig. 3. Velocity of the ABF. A linear frequency−velocity relationship is found at middle-ranged frequencies. At high frequencies the velocity drops after the step-out frequency and for low frequencies a sudden increase in the drift velocity is apparent. Below 2 Hz the drift velocity is larger than the forward velocity.

III. EXPERIMENTAL RESULTS

The ABF was driven over a wide range of frequencies above a smooth Si substrate and the forward and drift velocity were extracted from the recorded images. The frequency-velocity plot is depicted in Fig. 3. From the propulsion matrix (3) a linear relationship between the frequency input and the velocity of the ABF is expected.

$$v = -\frac{B}{A} \cdot \omega \tag{5}$$

Note that the matrix coefficient is $B < 0$ and $F = 0$. In Fig. 3, however, a linear relationship is only found at middle frequencies. A sudden decrease in velocity occurs at higher frequencies, and a sudden increase in velocity is evident at very low frequencies. It is apparent that the increase in the velocity at low frequencies occurs in the drift velocity, i.e. the velocity component perpendicular to the helical axis, while the forward velocity decreases almost linearly. For this particular ABF prototype the drift velocity dominates the swimming motion, i.e. the drift angle (φ) grows larger than 45 degrees, as the input frequencies drops below 2 Hz.

Additionally, the swimming motion of the ABF was recorded and at low frequencies a wobbling motion in sync with the magnetic field frequency was detected. The time-lapse images in Fig. 4 show the wobbly swimming motion of the ABF at three different input frequencies. The angle β describes the deviation of the helical axis of the ABF to the desired direction of motion and it is constant for a given frequency and decreases rapidly for higher frequencies as shown in Fig. 4. This resembles a precession phenomenon. The precession angle β was measured over a larger input frequency range and is depicted in Fig. 5 together with the drift angle φ. Both the wobbling and the drifting are significant at low frequencies and decrease for higher frequencies. The precession angle approaches almost zero, whereas the drift angle levels out and remains approximately constant at higher frequencies.

Fig. 6 shows experiments with a different ABF prototype inside a channel. The velocity of the ABF inside the channel did not significantly change compared with the velocity swimming above a flat surface. Fig. 6 (a) shows the ABF drifting slightly to the left as it advances along the channel (downward in image). Fig. 6 (b) shows the same ABF at a lower frequency where the wobbling and drifting is more prominent and where the drift propulsion is large enough for the ABF to roll along the sidewall and eventually to move out of the channel. The results imply that the non-ideal wobbling of the ABF at low frequencies enhances the drifting of the ABF to an extent that is not negligible. It is therefore desirable to optimize the ABF and avoid the wobbly swimming region in applications.

IV. DISCUSSION

A. *Step-out frequency*

The desired linear relationship between input frequency and output velocity is interrupted at the step-out frequency. This phenomenon is well understood and occurs when the drag, which increases with angular and translational velocity, grows larger than the maximum magnetic torque available [7]. At that point the ABF can no longer follow the rotation of the field, and the step-out frequency is reached. This limiting frequency is linearly dependent on the magnitude of the maximum magnetic torque that can be conveyed. The magnetic torque can be amplified by increasing the magnetic field strength or by increasing the volume of the magnetized head, which is shown in (4). Increasing the field strength has no further implications on the swimming behavior of the ABF and is only a matter of changing the design of the coil setup. Increasing the head size of the ABF results in higher step-out frequencies as well [2]. The bigger

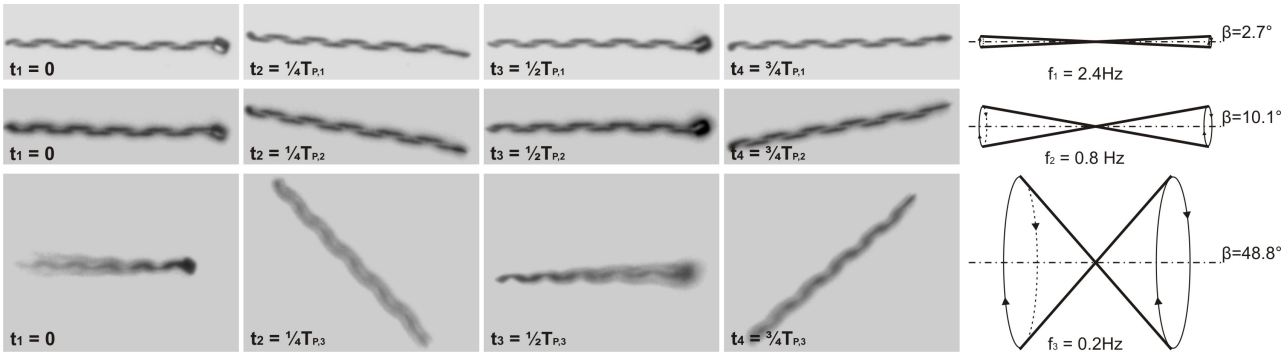

Fig. 4. Time-lapse of the ABF swimming at three different input frequencies $f_1 > f_2 > f_3$. The frequency of the precession is equal to the the input frequency. The precession angle β decreases rapidly for higher frequencies.

head, however, causes additional drag forces on the swimmer which moderate the gain of the additional torque. It has been shown that an optimal trade-off between torque maximization and drag minimization of the head can be found for a given tail [2].

B. Wobbling at low frequencies

The wobbling of the ABF at low Reynolds numbers is reminiscent of a spinning top that rotates stably around its axis at high frequencies but begins to wobble when the frequency decreases. While the gravitational pull induces a torque perpendicular to the rotational axis of a spinning top, an alternative explanation is required for the helical swimmer. Thus, the instantaneous force and torque equilibria are found, for a stable screw-type motion which consists purely of a rotation around and translation along the helical axis, using RFT established by Gray and Hancock [13]. The RFT divides the drag force on a filament into the force components along and perpendicular to the filament and relates these forces to the local velocities $u_{\parallel}$ and $u_{\perp}$. On an infinitesimally small length of filament, the parallel and perpendicular forces are

$$\begin{aligned} \mathrm{d}f_{d,\parallel} &= -u_{\parallel}\xi_{\parallel}\mathrm{d}s \\ \mathrm{d}f_{d,\perp} &= -u_{\perp}\xi_{\perp}\mathrm{d}s \end{aligned} \tag{6}$$

and the drag coefficients are given by [14]

$$\xi_{\perp} = \frac{4\pi\eta}{ln\left(\frac{0.36\pi R}{rsin\psi}\right)+0.5} \tag{7}$$

$$\xi_{\parallel} = \frac{2\pi\eta}{ln\left(\frac{0.36\pi R}{rsin\psi}\right)} \tag{8}$$

The rigid body motion of the ABF is described by $\vec{V} = (v_x,0,0)^T$ and $\vec{\Omega} = (-\omega_x,0,0)^T$, $\omega_x > 0$. Note that the analysis is for a left-handed helix. The coordinate systems used in the calculations are depicted in Fig. 7. The body coordinate system rotates around the x_I-axis with $\alpha = \omega_x \cdot t$ with respect to the inertial frame

$$R_{I\to B} = R_{X_I}(\alpha)$$

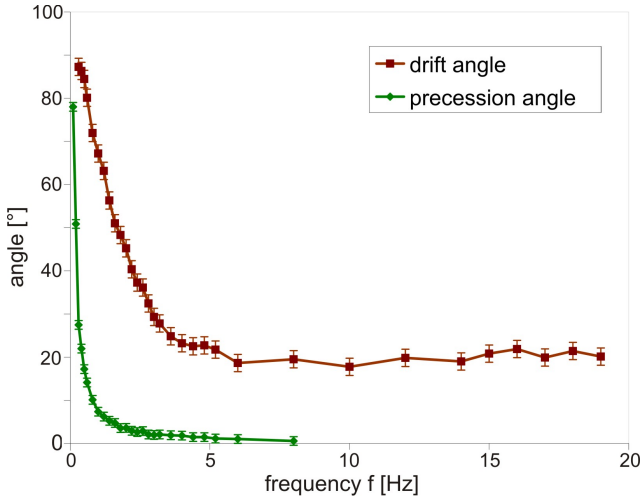

Fig. 5. The drift angle φ and precession angle β. The precession angle is measured from the axis to the lateral surface of the cone. Below 2 Hz $\varphi > 45°$ and the sidewise drift of the ABF is larger than the forward velocity. Both angles decrease exponentially for increasing frequencies.

and the local filament coordinate system can be described with respect to the body coordinate system with the rotational matrices

$$R_{B\to F} = R_{Y_C}(\psi)R_{X_B}(\theta).$$

The force and torque equilibria are found by integrating the drag forces (6) along the whole length of the helix.

$${}_I\vec{F}_{ext} = \begin{pmatrix} u_xR\Gamma/\tan\psi - \omega_xR^2\Xi/\tan\psi \\ 0 \\ 0 \end{pmatrix} \tag{9}$$

$${}_I\vec{\tau}_{ext} = \begin{pmatrix} u_xR^2\Xi/\tan\psi - \omega_xR^3\Lambda/\tan\psi \\ -u_xR^2\Xi\sin\alpha + \omega_xR^3\Lambda\sin\alpha \\ -u_xR^2\Xi\cos\alpha + \omega_xR^3\Lambda\cos\alpha \end{pmatrix} \tag{10}$$

where

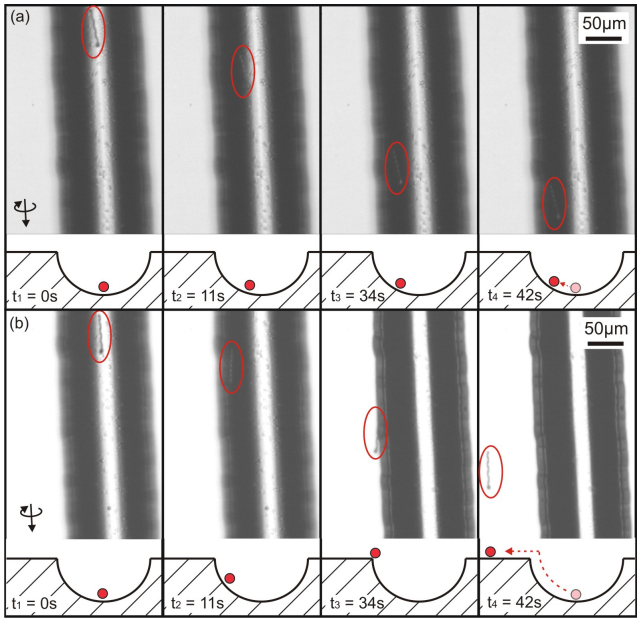

Fig. 6. Time-lapse images of an ABF inside a channel. (a) The ABF prototype swims along the channel (downward in image) and exhibits a slight drifting to the left. (b) For a lower frequency, the ABF wobbles and has an enhanced drift. The sidewise propulsion is large enough for the ABF to climb out of the channel.

$$\begin{aligned}\Gamma &= 2n\pi(\xi_\perp \cos^2\psi + \xi_\parallel \sin^2\psi)\sin\psi/\cos^2\psi \\ \Lambda &= 2n\pi(\xi_\perp \sin^2\psi + \xi_\parallel \cos^2\psi)\sin\psi/\cos^2\psi \\ \Xi &= 2n\pi(\xi_\perp - \xi_\parallel)\sin^2\psi/\cos\psi\end{aligned}$$

In the body coordinate system of the helix the torque is

$${}_B\vec{\tau} = \begin{pmatrix} u_x R^2 \Xi/\tan\psi - \omega_x R^3 \Lambda/\tan\psi \\ 0 \\ u_x R^2 \Xi - \omega_x R^3 \Lambda \end{pmatrix} \quad (11)$$

As expected, there is no resulting force perpendicular to the helical axis. It is apparent, however, that the torque required to sustain a pure translation along and rotation around the x-axis includes not only a torque along, but also perpendicular, to the axis. It can be regarded as an actuation and a stabilization torque, which is constant along the z_B-axis of the helix in the body coordinate system. If the drag force and torque are averaged over a full period $T_p = 2\pi/\omega_x$ of the rotation around the helical axis

$$\frac{1}{T_p}\int_0^{T_p} \vec{F}\,\mathrm{d}t \text{ and } \frac{1}{T_p}\int_0^{T_p} \vec{\tau}\,\mathrm{d}t$$

only the torque in the x_I-direction remains, which leads to the well-known propulsion matrix (3) [8].

From the non-averaged instantaneous torque equilibrium, it can be seen that no optimal screw-type swimming can be achieved unless a stabilization torque is applied to the helical swimmer. Additionally, if the design of the ABF is considered, it can be assumed that the wobbling is likely to be aggravated by the non-ideal placement of the head,

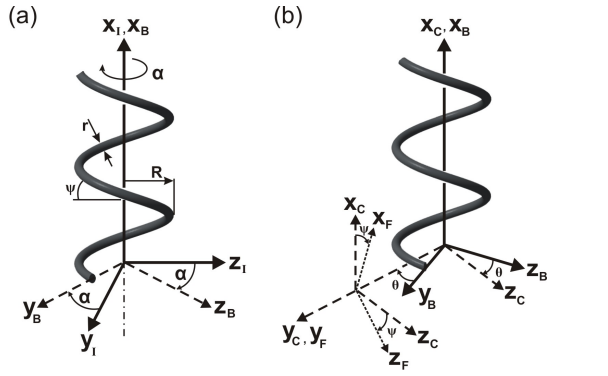

Fig. 7. (a) The body coordinate system is attached to the helical body and rotates with $\alpha = \omega_x \cdot t$ with respect to the inertial coordinate frame. (b) The local filament coordinate system is reached via a rotation around the helical x_B-axis and a rotation around the new y_C-axis with the constant helicity angle ψ.

which is located at a distance of radius R from the helical axis. Fluidic forces and any un-modeled magnetic gradient forces on the head are therefore applied off axis.

Alternatively, the ABF can be approximated by an elongated elliptical body [6] for which the drag coefficient for the torque around the long and short axis are according to the slender-body approximation, i.e.

$$\begin{aligned}\zeta_{ellipse,x} &= \tfrac{3}{16}\pi\eta ab^2 \\ \zeta_{ellipse,y} = \zeta_{ellipse,z} &= \frac{\pi\eta a^3/3}{\ln(2a/b)-0.5}\end{aligned} \quad (12)$$

where a and b are the major and minor axes, respectively [16]. From (12) it can be seen that the resistive torque around the long axis is larger than the resistive torque around the short axis of the ABF. The rotation around the x-axis is therefore preferred, and this acts in favor of helical swimming and provides resistance against the wobbling motion.

The two fluidic torques presented compete to stabilize and destabilize the rotation of the helix around its axis. It was shown in the experiments, however, that the precession angle changes with the frequency. We presume that this effect is attributed to inertial effects that have been neglected. In fact, the attenuation of the wobbling motion of 1-D nanostructures with higher rotating speed has also been observed for the self-assembled microparticles [17] and nanowires [18], that are actuated by rotating magnetic fields.

C. Drift

The drifting of microscopic swimmers occurs due to wall effects. The presence of a solid boundary increases the drag on a body, and this drag decreases with a growing distance between the body and the wall. Instead of having independent drag coefficients, such as (7) and (8), the local drag becomes a function of the distance h from the wall [19].

From Fig. 8 (a) it can be seen that the drag on a filament segment of the helical tail closer to the wall encounters a higher drag than a segment further away. This causes the helix to roll along the surface perpendicular to the helical axis.

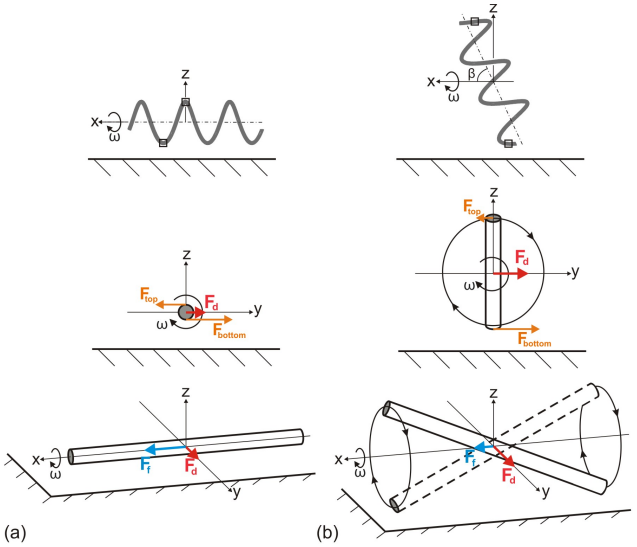

Fig. 8. Wall effects on the ABF. (a) Due to the drag force imbalance on the tail segments while rotating around the x-axis, the ABF rolls along the surface in the y-direction. (b) With the precession of the ABF propulsion in the y-direction grows larger while the desired movement in the x-direction decreases.

The influence of solid boundaries has been observed and analyzed for *E. coli* bacteria [15], [20]. The bacteria swim in circles due to the counter-rotation of their head and helical tail. The ABF has no such counter-rotation and is stabilized with the magnetic steering torque to keep its orientation while it is drifting [7]. The rolling speed increases linearly with the input frequency, as does the forward speed. This leads to a stable drift angle φ which was observed in Fig. 5 for high frequencies. The increase in the drift angle lies in the increased efficiency of the sidewise propulsion when the ABF wobbles (see Fig. 8). While the screw-type swimming becomes less efficient because of the non-optimal wobbling motion, the ABF pushes itself along the wall in a manner that resembles a paddling motion. This paddling near a surface is used for propulsion of other microdevices such as the colloidal microbeads [17] or nickel nanowires [21]. For the ABF, however, paddling enhances the undesired side drift. Indeed, paddling is so effective that the total velocity grows despite the decrease of the input frequency, and a local maximum is reached before the velocity goes to zero.

V. CONCLUSION

It has been shown that the frequency-velocity relationship can be divided into three different regions, i.e. the linear region, the step-out region and the drift-dominated region. In the step-out region at high frequencies the linear range is limited by the applicable torque. At low frequencies the ABF wobbles due to the helical shape of the tail itself and the off-axis placement of the head. It has also been shown that for larger precession angles the undesired sidewise drift increases. In the linear region the wobbling is attenuated and a screw-type swimming is achieved with a linear frequency-velocity relationship.

VI. ACKNOWLEDGMENTS

The authors thank Prof. Jake J. Abbott from the University of Utah for fruitful discussions on helical swimming and Donat Scheiwiller and Niels Quak from ETH Zurich for their technical support in microfabricating channels.

REFERENCES

[1] L. Zhang, J. J. Abbott, L. X. Dong, B. E. Kratochvil, D. J. Bell, and B. J. Nelson, "Artificial Bacterial Flagella: Fabrication and Magnetic Control", *Appl. Phys. Lett.*, vol. 94, art. no. 064107, 2009

[2] L. Zhang, J. J. Abbott, L. X. Dong, K. E. Peyer, B. E. Kratochvil, H. X. Zhang, C. Bergeles, and B. J. Nelson, "Characterizing the Swimming Properties of Artificial Bacterial Flagella", *Nano Lett.*, 2009

[3] T. Honda, K. I. Arai, K. Ishiyama, "Micro swimming mechanisms propelled by external magnetic fields", *IEEE Trans. Magn.*, vol. 32, pp. 5085-5087, 1996.

[4] A. Yamazaki, M. Sendoha, K. Ishiyamaa, T. Hayaseb, and K. I. Araia, "Three-dimensional analysis of swimming properties of a spiral-type magnetic micro-machine", *Sens. Actuators A: Phys.*, vol. 105, pp. 103-108, 2003.

[5] B. Behkam and M. Sitti, "Design Methodology for Biomimetic Propulsion of Miniature Swimming Robots", *J. Dyn. Syst. Meas. Control-Trans. ASME*, vol. 128, pp. 36-43, 2006.

[6] A. Ghosh and P. Fischer, "Controlled Propulsion of Artificial Magnetic Nanostructured Propellers", *Nano Lett.*, vol. 9, pp. 2243-2245, 2009.

[7] J. J. Abbott, K. E. Peyer, M. C. Lagomarsino, L. Zhang, L. X. Dong, I. K. Kaliakatsos, and B. J. Nelson, "How Should Microrobots Swim?", *Int. J. Robot. Res.*, vol. 28, pp. 1434-1447, 2009.

[8] E. M. Purcell, "Life at low Reynolds number", *Am. J. Phys.*, vol. 45, pp. 3-11, 1977.

[9] H. C. Berg and R. A. Anderson, "Bacteria swim by rotating their flagellar filaments", *Nature*, vol. 245, pp. 380-382, 1973.

[10] L. Zhang, E. Deckhardt, A. Weber, and D. Grutzmacher, "Controllable fabrication of SiGe/Si and SiGe/Si/Cr helical nanobelts", *Nanotechnology*, vol. 16, pp. 655-663, 2005.

[11] L. Zhang, E. Ruh, D. Grutzmacher, L. X. Dong, D. J. Bell, B. J. Nelson, and C. Schonenberger "Anomalous coiling of SiGe/Si and SiGe/Si/Cr helical nanobelts", *Nano Lett.*, vol. 6, pp. 1311-1317, 2006.

[12] J. J. Abbott, O. Ergeneman, M. Kummer, A. M. Hirt, and B. J. Nelson, "Modeling Magnetic Torque and Force for Controlled Manipulation of Soft-Magnetic Bodies", *IEEE Trans. Robot.*, vol. 23, pp. 1247-1252, 2007.

[13] J. Gray and G. J. Hancock, "The Propulsion of Sea-Urchin Spermatozoa", *J. Exp. Biol.*, vol. 32, pp. 802-814, 1955.

[14] J. Lighthill, "Flagellar Hydrodynamics", *SIAM Review*, vol. 18, pp. 161-230, 1976.

[15] E. Lauga, W. R. DiLuzio, G. M. Whitesides, H. A. Stone, "Swimming in circles: Motion of bacteria near solid boundaries", *Biophys. J.*, vol. 90, pp. 400-412, 2006.

[16] H. C. Berg, "Random Walks in Biology", *Princeton University Press* Princeton, NJ, 1983.

[17] P. Tierno, R. Golestanian, I. Pagonabarraga, and F. Sagues, "Controlled Swimming in Confined Fluids of Magnetically Actuated Colloidal Rotors", *Phys. Rev. Lett.*, vol. 101, 218304, 2008.

[18] P. Dhar, C. D. Swayne, T. M. Fischer, T. Kline, and A. Sen, "Orientations of Overdamped Magnetic Nanorod-Gyroscopes", *Nano Lett.*, vol. 7, pp. 1010-1012, 2007.

[19] C. Brennen and H. Winet, "Fluid Mechanics of Propulsion by Cilia and Flagella", *Annu. Rev. Fluid Mech.*, vol. 9, pp. 339-398, 1977.

[20] E. Lauga and T. R. Powers, "The hydrodynamics of swimming microorganisms", *Rep. Prog. Phys.*, vol. 72, 096601, 2009.

[21] L. Zhang, Y. Lu, L. X. Dong, R. Pei, J. Lou, B. E. Kratochvil, and B. J. Nelson, "Noncontact Manipulation of Ni Nanowires Using a Rotating Magnetic Field", *Proc. 9th IEEE Conf. on Nanotechnology (IEEE-NANO2009)*, 2009.